Electronic structure of the Cr(001) surface and Cr/MgO interface

M.-A. Leroy,[1,2] A. M. Bataille,[1] F. Bertran,[3] P. Le Fèvre,[3] A. Taleb-Ibrahimi,[3] and S. Andrieu[2]
[1]*Laboratoire Léon Brillouin, IRAMIS, CEA Saclay, 91191 Gif sur Yvette, France*
[2]*Institut Jean Lamour, Université de Lorraine, BP239, 54506 Vandœuvre-lès-Nancy Cedex, France*
[3]*Synchrotron SOLEIL, L' Orme des merisiers, 91192 Gif sur Yvette Cedex, France*
(Received 12 June 2013; published 25 November 2013)

We have undertaken a detailed study of the Cr surface and Cr/MgO interface electronic properties by symmetry- and angle-resolved photoemission spectroscopy on a Cr(001) surface covered or not with 1.2 monolayer MgO. For the bare Cr(001) film, the experimental bulk dispersions are in good agreement with the theoretical band structure, and characteristic antiferromagnetic features like the antiferromagnetic gap at the X point are observed. However, by covering the Cr film by 1.2 monolayer MgO, the observed experimental dispersions are strongly perturbed as a result of the existence of metal-induced gap states in the MgO film. By carrying out normal emission measurements, we detect two 2D localized states for the Cr(001) surface that persist at the Cr/MgO interface: a Δ_1 state at very low binding energy, which is usually associated with Cr surface magnetism, and an additional resonant Δ_5 state, which shall play a crucial role for transport and coupling in Cr/MgO epitaxial systems.

DOI: 10.1103/PhysRevB.88.205134 PACS number(s): 71.20.Be, 73.20.−r, 75.30.Fv, 75.70.Rf

I. INTRODUCTION

In the field of spintronics, Cr is mostly known for the discovery of the GMR effect in Cr/Fe multilayers,[1] where the Cr layer stands as a metallic spacer. However, its complex Fermi surface and the existence of spanning vectors plays a key role in the different oscillation periods of interlayer exchange coupling observed in these systems.[2–5] Its electronic band structure is also important for its itinerant antiferromagnetic order: an incommensurate spin density wave (SDW) phase arises from the nesting properties of its Fermi surface. As a model itinerant antiferromagnet, this material represents also a longstanding challenge for band structure calculations [density functional theory (DFT), tight binding], which still have difficulties in predicting the SDW state as ground state.[6,7]

Even more than calculating the bulk electronic structure, determining surface and interface states with adequate binding energies represents a challenge for calculations. These states are thought to have a strong link with the near-surface magnetism for the Cr(110) surface,[8] and with the surface magnetic order for the Cr(001) surface.[9] In epitaxial metal/oxide stacks (as Fe/MgO/Fe systems), Cr is usually used as a symmetry filter (some band symmetries are not present at the Fermi level)[10,11] and may also be an attractive counterelectrode to study spin-polarized transport, tunnel coupling,[12] or to test spin transfer torque in antiferromagnetic layers, with competitive properties compared to ferromagnetic layers.[13] To investigate these phenomena, the study of the electronic and magnetic properties of the Cr/MgO interface is a prerequisite.

A deeper knowledge of the bulk electronic band structure (binding energies and Fermi surface dimensions) and the characterization of Cr(001) surface and Cr/MgO interface states can be obtained through identification of electronic bands with high-resolution angle-resolved photoemission spectroscopy (ARPES). For the purpose of this study, this paper is organized as follows. First, we recall important theoretical and experimental results on the electronic structure and magnetism of Cr. We then provide information on the sample growth, on the ARPES technique, and on the data resolution and treatment. Our observations and results on the bulk Cr band structure at low binding energy, especially the paramagnetic and antiferromagnetic features, are described in the next section for two distinct measurement configurations. Afterwards, we describe and characterize the 2D localized states that we evidence both on a Cr surface and a Cr/MgO interface, providing in particular their dispersion and their symmetry. We finally discuss several points of interest of our findings: the observation of the magnetism through the band structure, the peculiarities of the dispersions observed for Cr/MgO that we link to the presence of metal-induced gap states, and the participation of the 2D states to the surface magnetism or the tunnel transport in epitaxial heterostructures.

II. STATE OF THE ART AND OPEN QUESTIONS

A. Theoretical background

As a 3d metal, the band structure of paramagnetic (PM) Cr is not a far cry from that of Fe: a good approximation is obtained by combining 3d tight-binding bands and sp nearly free electron bands folded in the Cr Brillouin zone (BZ),[17,18] featured in Fig. 1(a). This way, Lomer pointed out that the Cr Fermi surface exhibits an electron pocket centered at Γ and a hole pocket at H with large parallel sections that can be coupled through a nesting wave vector $\vec{Q}$ [see Fig. 1(b)]. Since the hole octahedron is slightly larger than the electron octahedron, $\vec{Q}$ is incommensurate with the reciprocal lattice parameter. Despite the small proportion of the charge carriers they represent, the contribution of Fermi surface electrons seems to be the driving factor for the existence of the antiferromagnetic (AF) order in Cr, conditioning, in particular, the period of its modulation.[19] Under 311 K, bulk Cr has a sinusoidally modulated antiferromagnetic order, called spin density wave [see inset in Fig. 1(b)], with small moments amplitude ($0.62\mu_B$ at 4 K, see Ref. 20), whose propagation vector $\vec{Q}'_{\pm} = (1 \pm \delta)\langle 001\rangle$ ($\delta = 0.048$ at low temperature) nearly equals the nesting vector $\vec{Q}_{\pm}$.[21] In alloyed or strained

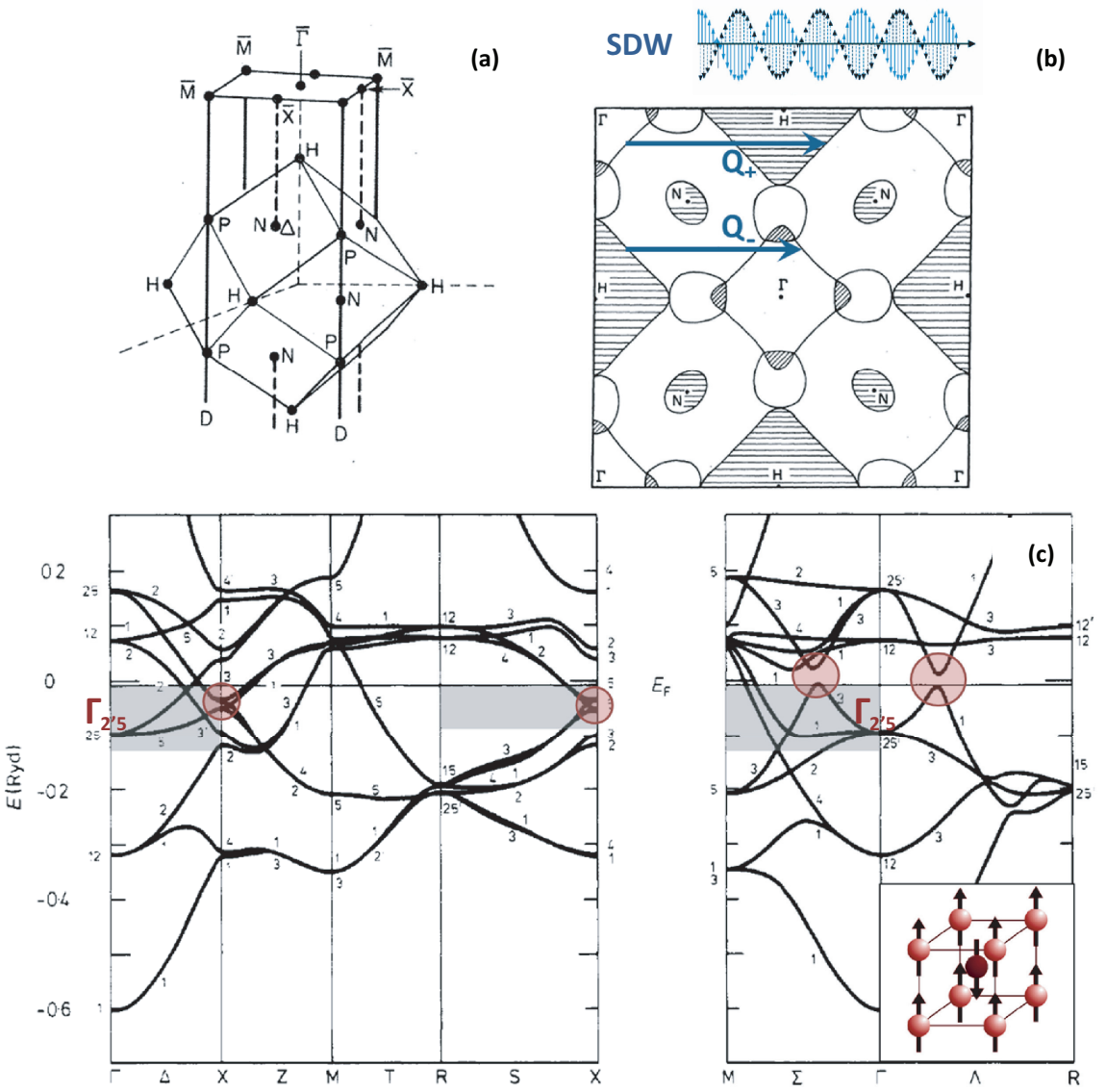

FIG. 1. (Color online) (a) Bulk Brillouin zone (first Brillouin zone) for paramagnetic Cr and its projection for the (001) surface.[14] (b) Fermi surface (001) slice for paramagnetic bulk Cr with nesting vectors $\vec{Q}_-$ and $\vec{Q}_+$.[15] Above, we show the associated SDW order with period $\Lambda_{SDW} \approx 20$ monolayers. (c) Band structure calculated for commensurate AF Cr[16] (represented as inset), the regions investigated in this paper are in gray. The sublattice magnetization obtained in this self-consistent calculation is smaller than the experimental value (here, $m = 0.32\mu_B$), leading to smaller energy gaps (emphasized by red circles). N and M, P and R are equivalent notations, respectively, in the PM and AF BZ.

Cr, a commensurate antiferromagnetic (AF) order is stabilized, where all AF moments are equal.[18,21]

As the magnetic moment of the SDW is almost entirely due to d electrons, a Stoner model with two exchange-splitted bands describes well the occurrence of an AF order.[16,17] In the lower band, the wave functions have the same spin polarization as the AF modulation whereas in the upper band, their spin polarization is reversed.[18] If only the lower bands are occupied (and thus the Fermi level is situated in the energy gap), a net polarization is obtained. This simple two-band model provides a good qualitative description of the electronic band structure calculated for commensurate AF Cr[16,18] [see Fig. 1(c)], where, at first order, the paramagnetic bands are folded back in the AF BZ (which consists in a cube). This leads to the apparition of gaps at the BZ edge [X point on Figs. 1(a) and 1(c)] and of accidental gaps along Σ and Λ that participate to the stabilization of the AF order (since E_F is in the gap). These gaps are situated at the electron octahedron edges of the paramagnetic Fermi surface [see Fig. 1(a)] that are destroyed by the nesting. If the bands are totally polarized at the gap, the width g of the AF energy gap is $g = Jm$, J being the effective Stoner interaction parameter and m the sublattice magnetization.

Concerning the Cr(001) surface, early calculations[22–24] have predicted that the magnetic moments on its last plane are ferromagnetically ordered, and that the value of these surface moments is enhanced (2.3–$3\mu_B$) in comparison to bulk moments. This surface ferromagnetism should survive the bulk Cr Néel transition at 311 K and possess a Curie temperature about 3–4 times higher than the Néel temperature

of bulk Cr.[22,23,25] The stabilization of this order originates from the increased electronic susceptibility at the surface. A surface state near the Fermi level appears in the calculations for a paramagnetic phase and is splitted by the surface exchange potential into two polarized surface states for a ferromagnetic surface.[22,23,25] Like for bulk states, the splitting of the states is proportional to the magnetic moment magnitude. In particular, band structure calculations expect a Δ_1 minority state at about 0.5 eV above the Fermi level (the minority character is given with respect to the orientation of the last plane moments).[25–28]

B. Experimental background

Many angle-resolved photoemission spectroscopy (ARPES) studies have been undergone to try to observe the characteristic features of the electronic structure described previously. Early studies by Gewinner[29] and Klebanoff[30] on Cr(001) surface and by Johansson[31] and Sakisaka[32] on the Cr(110) surface have provided energy dispersion curves at high binding energies, mostly for the Δ and Σ directions, that fit qualitatively the paramagnetic electronic structure. Hints for the AF structure have been detected through the symmetry of the structure at the X point.[30,33] Later, thanks to technological advances in ARPES setup, it became possible to observe low binding energy AF characteristics such as the band backfolding and the gap opening along the Σ axis, and to measure directly, with good accuracy, the Fermi surface[8,34,35] (in contrast to the very accurate but indirect information provided by de Haas-van Alphen measurements[36]).

Compared to band structure calculations, ARPES measurements are sensitive not only to bulk bands but also to surface localized states. The polarized minority state predicted by calculations has been observed by scanning tunnel microscopy (STM)[37] and was used to image the topological antiferromagnetism on the Cr(001) surface.[38,39] ARPES measurements have also detected a surface feature at low binding energies below the Fermi level[30,33] but its binding energy varies from a study to another and the symmetry of this state is still controversial.[39–41] We have carried out in an independent article a thorough study of this state, combining ARPES and polarized neutron reflectivity measurements.[9] The Cr(110) surface has also attracted interest for the sensitivity of its near-surface magnetism to surface modification (by hydrogen uptake), which could be linked to its low binding energy surface states.[8,42] Since we are interested in tunneling phenomena involving Cr/MgO epitaxial stacks, we have investigated the 2D localized states and their in-plane dispersion for the Cr(001) surface and the Cr/MgO(001) interface, as surface states can be modified by the presence of a top layer.[43,44]

In our survey, we have taken advantage of the available incident photon energy range, linear polarization orientations and high energy resolution on the Cassiopée beamline to supply up-to-date low binding energy, symmetry-resolved dispersion curves for Cr(001) films. Our extensive experimental data for bulk bands will enable to complete earlier studies on the Cr bulk band structure and to lead a thorough comparison of the experimental dispersions with the calculated band structure. In addition, we will be thus able to differentiate accurately bulk from surface features, definitely establish the symmetry of already evidenced surface states, observe additional ones, and provide for both their in-plane dispersion as well as identify them as pure surface states or resonances. Finally, the investigation of the Cr/MgO interface is required to interpret the properties of Cr/MgO epitaxial heterostructures, and we will provide a detailed report on its peculiar electronic properties.

III. EXPERIMENTAL METHODS

High-resolution angle-resolved photoemission measurements were carried out on the Cassiopée beamline at the Soleil synchrotron, in the ARPES setup connected with the growth chamber, where Auger spectroscopy and RHEED enable an adequate control of the surface quality.

A. Samples growth

A Cr(001) layer was deposited onto a MgO(001) substrate by molecular beam epitaxy after prior annealing and outgasing of the substrate. The relation of epitaxy for this stack is MgO(001)[110]//Cr(001)[100]. The sample was annealed at high temperature (about 650 °C) to improve its crystallinity and decrease the surface roughness. The Cr surface was then cleaned by repeated annealing and Ar^+ bombardment cycles to obtain a contaminant-free surface, ascertained by the absence of $c(2 \times 2)$ reconstruction in RHEED patterns. The concentration of O, N, or Ar contaminants on the surface as probed by Auger electron spectroscopy was below the detection threshold, while for C (which is the most difficult impurity to remove from the Cr surface[45]), a very weak peak remained, which indicates the presence of C contamination (far less than a half monolayer).

For the Cr/MgO(001) sample, the growth process was the same, and an ultrathin MgO layer was additionally deposited onto the Cr surface. Using the calibration of the MgO deposition with reflection high-energy electron diffraction (RHEED) oscillations, the MgO thickness was set to 1.2 ML($\pm$0.1 ML), which was verified by measuring the intensity of the Cr 3p and Mg 2p core level peaks on our Cr/MgO sample. According to our experience in growth of such systems, the Cr layer (even a 1-ML-thick layer) is not oxidized at the interface with MgO with this growth recipe. Namely, using XPS at the Cr 2p edge, no sign of oxidation was observed for a Cr monolayer covered with MgO, with respect to a bare Cr monolayer.

X-ray diffraction and reflectivity were carried out on the Cr/MgO sample after the ARPES experiments. We determined the thickness of the Cr film (50 nm) and the epitaxial deformation in the Cr layer: 0.09% for the in-plane parameter and 0.06% for the out-of-plane parameter. This weak strain is in agreement with that usually measured on our Cr thin films grown with the same recipe, with reproducible structural and magnetic properties.

B. Angle-resolved photoemission technique

1. Setup and experimental resolution

We used a monochromatic incident beam of energy ranging from 20 to 100 eV with 0.5 eV steps, the linear polarization could be oriented in the $(\bar{1}10)$ plane (p polarization), or perpendicular to it, along $[\bar{1}10]$ (s polarization) [see Fig. 2(a)].

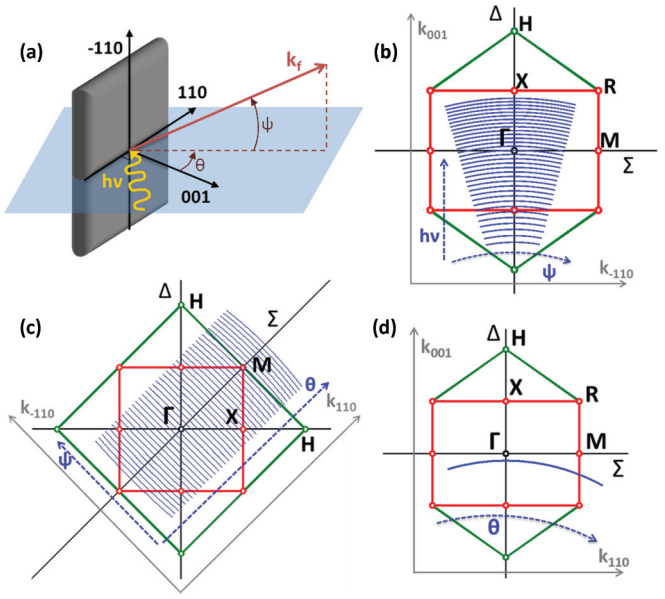

FIG. 2. (Color online) (a) Geometry of the photoemission measurement. The blue plane marks the $(\bar{1}10)$ mirror plane, the orange corrugated line represents the incident polarized light beam, and the red vector the final wave vector of the photoelectron in vacuum. (b) and (c) Measurement configurations and portions of the (110) (b) and (001) sections (c) of the BZ explored by the two types of scans (in blue, every fifth scan). In green is the paramagnetic BZ, in red is the antiferromagnetic BZ, and their high symmetry points and directions. (d) Portion of the $(\bar{1}10)$ BZ explored by a scan at constant ψ and $h\nu = 60$ eV (blue line). It is not a straight line passing through the Γ point but a curved trajectory departing from the Σ direction toward the ΓR direction.

The sample holder provided a rotation of the sample around the $[\bar{1}10]$ axis (θ angle) and enabled to cool down the sample to 150 K (where the surface moment should be the highest[23]) or heat it to 370 K (above the theoretical Néel temperature). A wide angle lens energy analyzer allowed detecting photoelectrons making $+/-15^\circ$ angles away from the $(\bar{1}10)$ mirror plane [ψ angle on Fig. 2(a)]. The pressure in the growth and ARPES chambers was kept in the 10^{-11} mbar range.

The measurements described in Figs. 2(b) and 2(c) were carried out with 0.2° θ steps and 0.045° ψ steps, corresponding to steps along k_{110} and $k_{\bar{1}10}$ of respectively 0.013 and 0.003 Å^{-1} at the typical photon energy of 60 eV. The resolution on these wave vectors components is of the same order of magnitude as the steps. The 0.5 eV steps used for the incident photon energy provided nonconstant k_{001} steps reaching 0.015 Å^{-1} at 60 eV and 0.023 Å^{-1} at most. The k_{001} resolution is far better (of the order of 10^{-4} Å^{-1}). The photoelectron kinetic energy step was 10 meV, and the obtained binding energy resolution is governed by the resolution of the monochromator and by the pass energy and slit size of the detector. At an incident photon energy of 60 eV, it reached 8.6 meV for the Cr sample and 14 meV for the Cr/MgO sample, and at most (for the highest photon energy) 12.5 meV for Cr and 21 meV for Cr/MgO. This very good resolution is the reason why such sensitivity is achieved on the low binding energy features, in comparison to early works for which the typical energy resolution is 150 meV.[30] Since our measurements were carried out at 150 and 370 K, thermal broadening is the dominant factor governing the peak width of the detected features.

2. 3-step model for data interpretation

We interpret our data using the so-called 3-step model.[48,49] (1) An electron is optically excited from an initial state to a final state of the crystal by absorption of a photon. The momentum and total energy of the [electron + photon] system are conserved during this step (to within a reciprocal lattice wave vector $\vec{G}$). The authorized transitions (and hence possible initial states) are imposed by dipolar selection rules, taking into account the photon polarization and the constrained symmetry of the final state[46,47](see Table I). With this choice of photon energy, we have studied the excitation of valence electrons, situated at low binding energies.

(2) The excited electron travels as a wave packet toward the sample surface and can undergo inelastic scattering by the crystal, limiting thus its elastic escape depth. In our samples, the escape depth from the Cr layer, which strongly depends on the electron kinetic energy (and thus on the incident beam energy), typically reaches 3 ML for bare Cr and about 2 ML for Cr covered with 1.2 ML MgO (see Fig. 3).

(3) The photoelectron can escape the surface potential if the normal component of its kinetic energy is higher than the material work function ϕ (about 4 eV for our Cr samples). In this electron refraction process, the normal wave vector component (k_{001}) is not conserved, while the in-plane components are. In normal emission, the final state of the detected electron in vacuum shall be totally symmetrical, while for mirror plane emission, it shall be even with respect to the mirror plane[46,47] (see Table I). To retrieve the complete initial wave vector information, we chose to approximate the final state dispersion in the crystal by a nearly free electron dispersion in the reduced BZ, with maximal binding

TABLE I. Authorized symmetries of electronic initial states for the different measurement configurations, deduced from Refs. 46 and 47.

		Initial state	
	Final state	*s* polarization ($\|\|[\bar{1}10]$)	*p* polarization ($\|\|[001]$; $\|\|[110]$)
Δ [001] normal emission	Δ_1	Δ_5	Δ_1; Δ_5
Δ [100] in (010) mirror plane emission	Δ_1, Δ_5, Δ_2	Δ_1, Δ_5, Δ_2, Δ_2'	Δ_1, Δ_5, Δ_2, Δ_2'
Σ [110] in normal emission	Σ_1	Σ_4	Σ_3; Σ_1
Σ $[\bar{1}10]$ in (110) mirror plane emission	Σ_1, Σ_3	Σ_1, Σ_3	Σ_1, Σ_3; Σ_2, Σ_4
Σ [110] in $(\bar{1}10)$ mirror plane emission	Σ_1, Σ_3	Σ_2, Σ_4	Σ_1, Σ_3; Σ_1, Σ_3

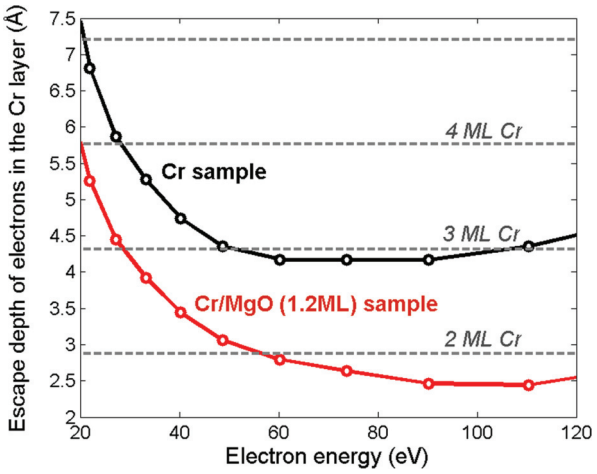

FIG. 3. (Color online) Escape depth of the electrons from the Cr layer for bare Cr and Cr/MgO (1.2 ML) as a function of their kinetic energy.[50]

energy E_0 corresponding to the bottom of the free electron band.

Within this model, one obtains the electron initial energy E_i, binding energy E_b, and momentum k as a function of the photoelectron kinetic energy E_c, wave vector angles ψ and θ in vacuum:

$$E_i = E_c - h\nu + \phi = -E_b, \tag{1}$$

$$k_{001} = \sqrt{\frac{2m}{\hbar^2}E_c \cos^2(\psi)\cos^2(\theta) + V_0}, \tag{2}$$

$$k_{110} = \sqrt{\frac{2m}{\hbar^2}E_c}\cos(\psi)\sin(\theta), \tag{3}$$

$$k_{\bar{1}10} = \sqrt{\frac{2m}{\hbar^2}E_c}\sin(\psi). \tag{4}$$

V_0 is the inner potential and is deduced from the binding energy of the bottom of the free electron band E_0: $V_0 = E_0 + \phi$.

We have carried out two kinds of measurement series for each sample, at both temperatures: scans at different photon energies $h\nu$ for (110) mirror plane emission (at $\psi = 0$, it reduces to normal emission), displayed in Fig. 2(b), and scans at a fixed incident photon energy (60 eV) in off-normal emission configuration [which reduces at $\psi = 0$ to $(\bar{1}10)$ mirror plane emission], displayed in Fig. 2(c). Theses trajectories in the reciprocal space enable to explore large portions of the AF Brillouin zone $(\bar{1}10)$ and (001) sections. By extracting and interpolating appropriate scan directions, one can deduce the dispersion relations for the major high symmetry directions of the BZ, e.g., the normal Δ direction, the in-plane Σ, S, and Δ directions, and obtain the Fermi surface (001) and (110) slices. The measured dispersions will be compared qualitatively with self-consistent band structure calculations for antiferromagnetic bulk Cr by Skriver *et al.*[16] [see Fig. 1(c)] and calculations of the paramagnetic Fermi surface by Laurent *et al.*[15] We have focused our study on low binding energy features as we expect interesting 2D states and features characteristic of the magnetism to be situated within these energy ranges. Moreover, the presence of MgO shall not disturb the observed bulk bands as the measured energies lie in the MgO gap (7.8 eV).

C. Data treatment

2D energy distribution maps (EDM) are compared with theoretical calculations, and taking into account symmetry selection rules in the measurement configurations (see Table I), the bands are identified. By determining for each configuration (normal emission or mirror plane emission) the possible symmetries of the final state, and using dipolar selection rules for s and p incident photon polarizations,[47] the authorized initial-state symmetries are determined.

As evidenced in Figs. 2(b) and 2(c), dispersions along the high symmetry directions can be obtained through interpolation of the 1D scans. For the (001) reciprocal space plane, we used the measurements represented in Fig. 2(c), which provide a reciprocal space map deviating yet slightly from the (001) plane to form an onion peel shape. At nonzero ψ and θ angles, the normal k_{001} wave vector moves away from the ΓXM plane [see Fig. 2(d)]. It explains partly the deviation of the experimental with respect to the calculated dispersions for in-plane wave vector directions.

To carry out the interpolation of the 3D data, 5-meV steps and 0.005 $Å^{-1}$ steps are, respectively, used for the binding energy and for the wavevector. For the EDM presented subsequently, data are generally integrated on ± 0.025 $Å^{-1}$ along the wave vector direction perpendicular to the maps. Fermi surface maps use integrations of ± 25 meV with respect to the Fermi level. The Fermi level is set by fitting the Fermi-Dirac distribution on the energy distribution curves (EDC) and a value of about $\phi = 4$ eV for the Cr work function is thus obtained. The color scale is linear for each figure and generally no normalization has been used apart for the scans with a variation of the photon energy (leading to nonconstant band cross sections). The Fermi surface (110) slice was normalized to the same reciprocal lattice slice at high binding energy, and the k_{001} EDM was normalized to the maximum intensity for each scan at constant k_{001} in order to highlight the bulk band dispersion.

To obtain surface states dispersions, we have taken advantage of the similarity of their in-plane dispersion at any photon energy (and thus normal wave vector k_{001}) to gain intensity on the surface feature. After verifying that they are identical at any k_{001}, we summed these dispersions on a wide range of k_{001} values. For the "Δ_1" state, which is detected with only one polarization, we have additionally normalized the map recorded with p polarization with that recorded with s polarization in order to remove the bulk band visible in both polarizations. The obtained map is then divided by the Fermi-Dirac distribution to gain access to features slightly above the Fermi level (50 meV above E_F at 150 K).

The binding energy of the states presented in a chart were obtained by fitting the EDC with the product of a pseudo-Voigt function (for the peak) and of a Fermi-Dirac distribution whose temperature was fitted. The Fermi surface dimensions and group velocities were obtained by fits of the peaks on constant binding energy slices above and below the Fermi level.

IV. OBSERVATIONS AND RESULTS

A. Bulk Cr band structure

In this part, we address a description of the Cr bulk electronic band structure, and discuss the features that are shared by both the Cr and the Cr/MgO samples. Exploiting the high resolution in energy and angles, and the possibility to switch the incident light polarization, we identify the magnetic characteristic dispersions and provide accurate values of the binding energies, dimensions of the Fermi surface, and electron velocities at the Fermi level.

1. In-plane wave vector measurements

It is possible to gain a good knowledge of the band structure near the Fermi level using the scans carried out at a constant incident photon energy of 60 eV [see Fig. 2(c)]. This energy corresponds for $k_{\parallel} = 0$, to $k_{\perp} = k_{001} = 3.86\pi/a$, which is near the zone center Γ, situated at $k \equiv 0[4\pi/a]$. The dispersions along Δ and Σ, the two principal high symmetry directions in the (001) plane, are presented for a p-polarized incident beam that excites the bands of all symmetries for the Δ direction in (010) mirror plane emission but only Σ_1 and Σ_3 symmetries for the Σ direction in ($\bar{1}10$) mirror plane emission (see Table I). The results of these measurements recorded at 150 K for both Cr(001) and Cr/MgO(001) samples are presented in Fig. 4: maps of the Fermi surface (001) section are displayed in Figs. 4(a) and 4(b) and energy distribution maps along the high symmetry directions Σ (ΓM) and Δ (ΓX) indicated on the Fermi surfaces are displayed in Figs. 4(c)–4(f). The Fermi surface edges and experimental dispersions (corresponding to high-intensity regions) are compared to the theoretical Fermi surface (001) plane for paramagnetic Cr[15] and to calculated dispersions for the commensurate AF band structure.[16] The additional sections present in AF band structures compared to paramagnetic Cr are underlined by dashed lines.

a. Paramagnetic features. As a first step, we will restrict ourselves to a comparison of the experimental band structure with the calculations for paramagnetic Cr. Some characteristic features on the Fermi surface are well detected for both samples: an electron square centered at Γ, which corresponds along Δ to the intersection of the Δ_2' band with E_F and along Σ to the Σ_3 band intersection; a hole ellipse centered at M, which corresponds along Σ to the intersection of the Σ_1 band with the Fermi level. There are also hints of the presence of electron balls at X and of an edge of the hole square [that should be centered at H, see Fig. 1(a)], however, the dimensions of the balls seem not to match very well their reported paramagnetic dimensions. As exposed previously in the data treatment section [see Sec. III C and Fig. 2(d)], the constant photon energy map does not provide a perfect (001) section of the reciprocal space but more an onion-peel-shaped map. It explains why the measured dimension of the hole ellipse along Σ is smaller than its reported value, and why for the experimental Δ dispersion, the Δ_5 band is not well reproduced. On this scan, the intensity observed at high binding energies should be associated to this deviation from the Δ direction, as in the Σ [101] direction the highly dispersive bent down band Σ_2 exists [it is indicated by the notation Δ_5/Σ_2 in Figs. 4(e) and 4(f)].

Put aside these deviations, the shape of the experimental dispersion curves for the Σ_3 (paramagnetic part) and Δ_2' bands matches well the calculated dispersions. The Σ_1 experimental band is much more dispersive near Γ than its theoretical counterpart, and is merged with the Σ_2 theoretical band [indeed in Figs. 4(c) and 4(d), the Σ_1 band is responsible for all the high binding energy intensity]. This is also observed for scans along the [$\bar{1}10$] Σ direction in the (110) plane (interpolated from scans at different photon energies).

Besides, the binding energies obtained from calculations are overestimated, and we have applied a scaling factor of 0.58 on the theoretical bands to recover our experimental binding energy for the $\Gamma_{2'5}$ point [indicated in red in Fig. 1(c)]. The binding energies, group velocities at E_F, and dimensions of the Fermi surface features are supplied in Table II (for Fermi surface dimensions, we provide only the values extracted from nondistorted scans).

b. Antiferromagnetic features. Since the film thickness is large enough to prevent finite size effects, and the strain and defect concentration are low (according to our x-ray diffraction measurements), a commensurate AF order if not an incommensurate SDW order, should be present in our samples at 150 K. Thus we expect to detect the specific features of the AF band dispersions (in dashed white lines), which stem from the folding of the PM BZ into an AF BZ (ΓX and XH bands superimpose along Δ and ΓM and HM bands along Σ).

For the Cr/MgO sample, the additional section of the Σ_3 band, which is characteristic of AF ordering, is indeed observed [see Fig. 4(d)]. Along the Δ direction, the Δ_5 band splitting at the X point can be spotted from the presence of an electron band near the Fermi level [see Fig. 4(f)]. This gap will be examined more precisely thanks to normal emission measurements. The edges of the electron square on the Fermi surface shall be destroyed by the nesting [depicted on Fig. 1(b)] because of the gap at the Fermi level associated with the band hybridization. The intensities along the theoretical edges are indeed fairly low for the Cr/MgO sample apart along the Σ directions, where, as will be described in the following, 2D localized states bring an intense contribution. Besides, it is natural to keep some intensity at these edges if the lower band of the gap reaches the binding energy integration range for the Fermi surface ($\pm$25 meV).

The scans recorded on the Cr sample display hints of the presence of a gap at the X point and symmetrical dispersion with respect to this high symmetry point. However, along Σ, the Σ_3 band backfolding is not detected and there is residual intensity on the electron square edge. It can be concluded that, even if the AF order is present in this sample, the nesting is possibly not perfect, leading to large unnested sections of the Fermi surface. It could be due to a lower quality of the surface of this sample (higher roughness), as we probe here the very last monolayers (about 3 ML). It is thus necessary to examine the dispersion along several high symmetry directions before deducing the magnetic phase of this layer.

2. Out-of-plane wave vector measurements

One of the interest of carrying out normal emission measurements is to identify 2D localized states but it is also possible to gain further information on the bulk band structure.

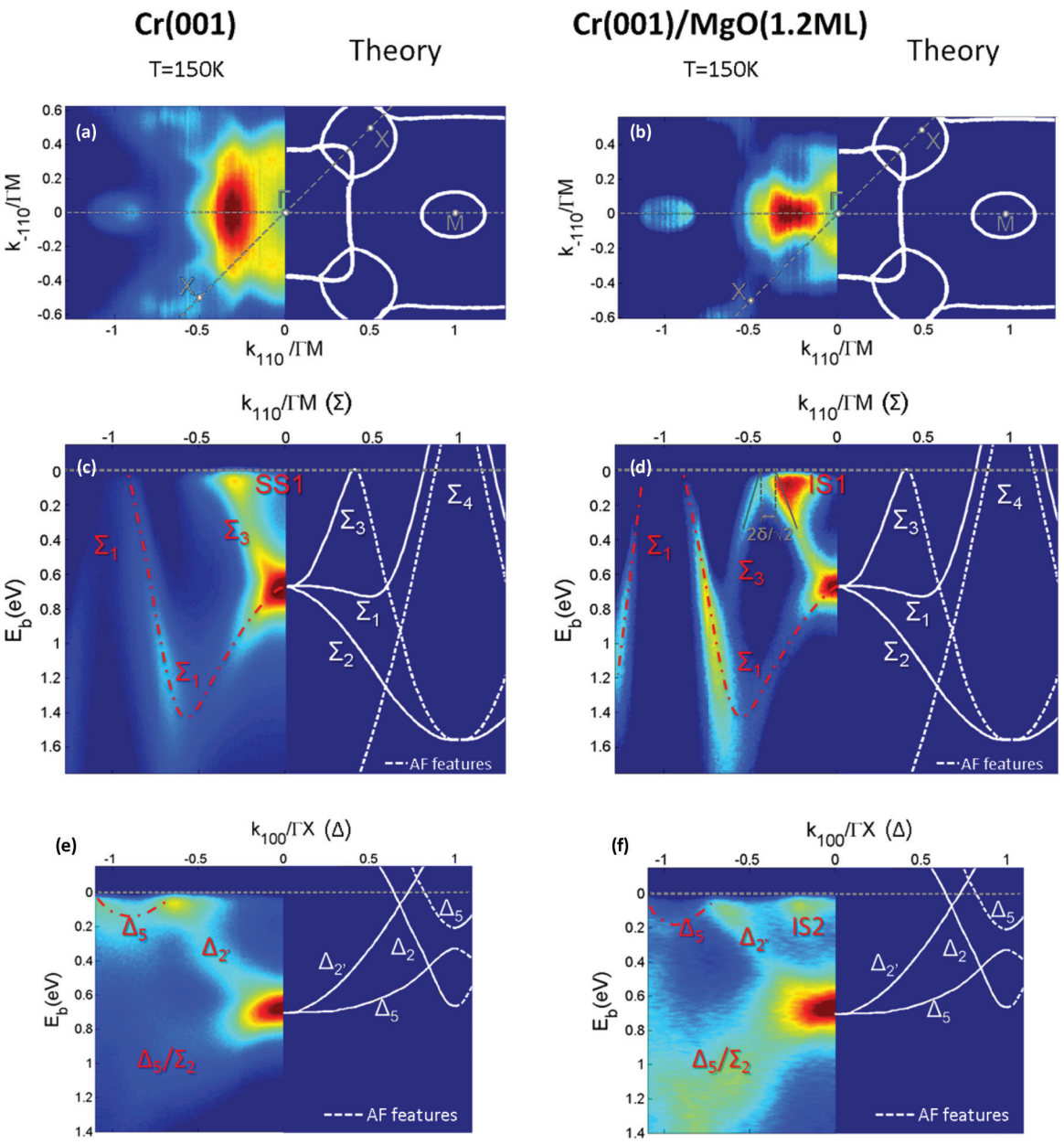

FIG. 4. (Color online) Bulk band structure for in-plane wave vectors extracted from the measurements described in Fig. 2(b) at 150 K, with p polarization at $h\nu = 60$ eV. The left column gathers data for the bare Cr sample and the right column for the MgO covered Cr sample. (a) and (b) Fermi surface (001) planes. The white contour is the calculated Fermi surface (001) plane for paramagnetic Cr, see Ref. 15. The gray dashed lines represent the high symmetry directions Σ and Δ for which the experimental dispersions are given in (c) and (e) for Cr and (d) and (f) for Cr/MgO. The white lines are the calculated dispersions for commensurate AF Cr, see Ref. 16, with a scaling coefficient 0.58 (see text for details); the additional sections present in AF compared to paramagnetic Cr are underlined by dashed lines. The bands and their symmetry representations are indicated in white for the theoretical calculation and red for the experimental interpretation (red dashed-dotted lines are guidelines for eyes). The notation "SS" stands for surface state, whereas "IS" stands for interface state. The determination of δ is illustrated in (d) (see text for details).

Scanning the normal k_{001} wave vector direction is obtained by varying the photon energy $h\nu$ [see Fig. 2(b)], which modifies also the investigated depth in the sample (see Fig. 3): the escape depth is minimum on the 60–120 eV incident photon energy range. The normal wave vector component is calculated using Eq. (3), but the inner potential V_0 has to be experimentally determined. To this purpose, we have set the Γ point ($k_{001} = 4\pi/a$) at the symmetry center of the bulk Δ_5 band, and the X point ($k_{001} = 3\pi/a$) at the wave vector for which the Δ_5 band splitting is the smallest [see Fig. 5(b)]. With this method, we obtain $V_0 = 11.4$ eV, which puts the bottom of the free electron band at $E_0 \approx 7.4$ eV (with $\phi \approx 4$ eV). This is in good agreement with the values reported in the literature ($V_0 = 12$ eV from calculations for AF Cr,[16] $V_0 = 10.8$ eV as experimental value[29] and $E_0 = 7.72$ eV, see Ref. 15, and 7.04 eV, see Ref. 18, from calculations). In these measurements

TABLE II. Experimentally measured features of the Cr band structure (in parenthesis the values for the Cr/MgO sample), dimensions of Fermi surface features, velocities at the Fermi level, and binding energies at high symmetry points.

Features	Direction in the BZ	Dimensions (Å^{-1})	Group velocity at E_F (10^5 m/s)
Electron octahedron edges	along ΓX	0.76 (0.76)	1.7 (1.9)
	along ΓM	0.52 (0.54)	2.65 (2.65)
2D state "SS1"	along ΓM	0.54	0.55
2D state "SS2"	along ΓX	(0.27)	(1.9)
	along ΓM	0.28 (0.29)	2.42 (2.56)
Features	Representation	Binding energy (eV) at 150 K	
Δ_5 and $\Delta_2^{'}$ bulk bands	$\Gamma_{25}^{'}$	0.68 (0.65–0.67)	
AF gap at X, bottom band	X_5	0.30 (0.40)	
AF gap at X, top band	$X_5^{'}$	0.06 (0.10)	
2D state "SS1"	$\Gamma_{12}^{'}$	0.051 (0.059)	
2D state "SS2"	Γ_{15}	(0.39)	

(but more specifically for 2D states investigations), we have taken advantage of the availability of s and p polarizations of the photon beam. The authorized initial states for the Δ direction in normal emission and for the XR direction (of same symmetry group as the Σ direction) in ($\bar{1}10$) mirror plane are given in Table I.

a. Cr sample. In normal emission, the only detected bulk band is that of Δ_5 symmetry, thus on the Fermi surface (110) slice displayed in Fig. 5(a), the extremities of the electron octahedron along Δ, which stem from $\Delta_2^{'}$ bands are not observed. The energy distribution map (EDM) in normal emission along the Δ direction is presented in Fig. 5(b) for s polarization and shows that the Δ_5 band has the same characteristic shape—very flat near the zone center—as calculated. The flat dispersion of this bulk Δ_5 band has sometimes lead to erroneous interpretations of this feature as a surface localized state. At the BZ edge (X point at $k_{001}/\Gamma X = -1$), the band is splitted into a down part, which reaches its minimum binding energy at X, and an up part near the Fermi level, detected on a small wave vector range near X. It can be recognized as the anticrossing of the Δ_5 bands due to BZ folding, which leads to the opening of a Brillouin zone edge gap.

In the in-plane XR direction, normal to the Δ direction, the gap at X is noticed by the energy shift at $k_{\bar{1}10} = 0$ between two parabolas (there is a lack of intensity near X between 0.1 and 0.3 eV binding energy). The energy distribution curve (EDC) at X enables the determination of the gap energy width at 150 K [see Fig. 5(f)]. The gap is estimated to 0.24 eV at 150 K and 0.18 eV at 370 K by fitting the up-band and down-band peaks with Lorentzian functions [the dispersion along Δ at 370 K is shown in Fig. 5(c)].

The Δ dispersion in Figs. 5(c) and 5(d) is not symmetrical with respect to the X point and shows a sharp discontinuity on the left part of X for a photon energy of 30 eV. This anomaly is also present in the work of Nakajima *et al.*[33] and stems from the failure of the free electron final state approximation at low incident photon energies, which is usual for Fe or Cr at these photon energies.[14,31] Indeed, for high final electron energies, the agreement between the real dispersion and a free electron dispersion is fairly good, but at lower electron energies (about 30 eV here), the real final bands depart too much from this estimation and the k_{001} wave vector determined in this approximation becomes inaccurate. In particular, two different bands shall be available as final states for one incident beam energy, leading to the excitation of states of the same band but of different k_{001} with the same photon energy. Here at 30 eV, a state of initial k_{001} near X is excited ($k_{001} = -1.12\Gamma X$), but also another situated near the zone center. Near 20 eV, on the left extremity of the map 5(b), the measured binding energies are that of the initial wave vectors near X. Accurate band structure calculations up to 30 eV above the Fermi level (which go beyond the scope of this paper) are necessary to confirm this interpretation and determine initial wave vectors at low incident photon energies.

b. Cr/MgO sample. Concerning the in-plane measurements, it is not expected that the presence of a MgO overlayer shall modify drastically the Cr bulk band structure (even if it seems that AF features are more easily detected for the Cr/MgO sample, possibly because of a higher interface quality). However, when scanning normal wave vectors by varying the incident photon energy, important differences are observed between the dispersions for bare Cr (see Fig. 5) and for Cr covered with MgO (see Fig. 6). As displayed in Fig. 6(a) with s polarization, the intensity observed up to 60 eV is approximately consistent with the dispersion of the Δ_5 band of bulk Cr [see Fig. 5(b)], with the gap at X (at $h\nu \approx 33$ eV) giving rise to near E_F features. Yet for photon energies higher that 60 eV, features of symmetry Δ_5 (only symmetry visible with s polarization) appear clearly near E_F, which are underlined by a dashed red line. They can neither be accounted for by the bulk band structure (a Δ_5 band shall appear near the Fermi level only at the X points, near 33 and 106 eV) nor by the Cr surface structure (the surface Δ_5 state is observed at about 0.4 eV below E_F). Moreover, an apparent transfer of intensity of the bulk band to lower binding energies takes place starting from 70 eV, which would correspond to k_{001} between $4.13\Gamma X$ and $4.87\Gamma X$ (using $V_0 = 11.4$ like for the Cr sample and as determined from the first X point at $3\pi/a$). This is hence not consistent with the expected inflection of the Δ_5 band at the X point for $k_{001} = 5\pi/a$. This transfer of intensity is more easily detected above 70 eV, as the bulk Δ_5 band is less intense at these energies.

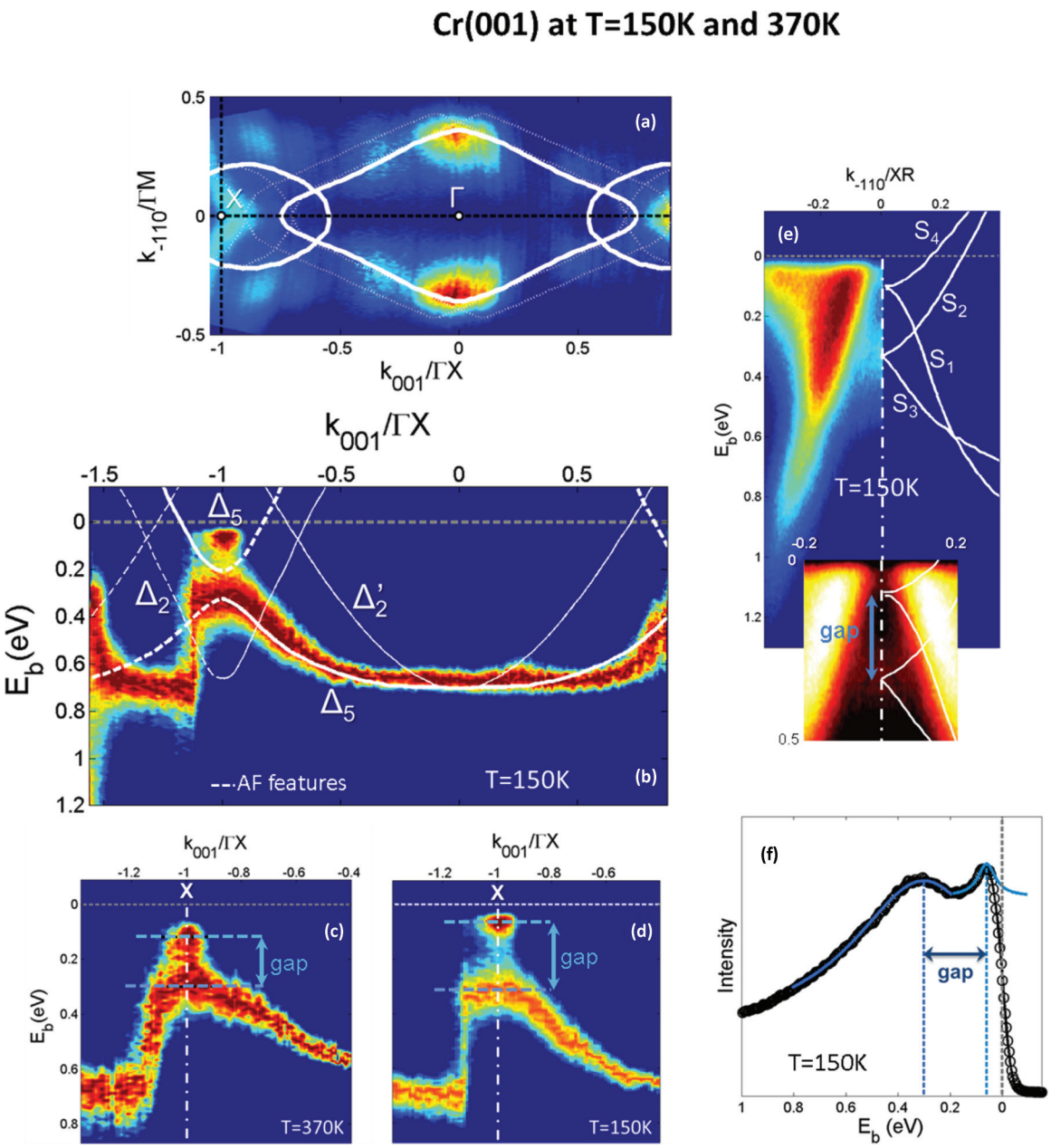

FIG. 5. (Color online) Bulk band structure for out-of-plane wave vectors extracted from the measurements described in Fig. 2(c), recorded with s polarization at 150 K [apart from (c) recorded at 370 K]. (a) Fermi surface (110) slice. The white contour is the calculated Fermi surface (110) plane for paramagnetic Cr, and, in particular, the electron octahedron centered at Γ, see Ref. 15. The dashed lines represent the contours translated by nesting vectors $\vec{Q}_+$ and $\vec{Q}_-$ and, in particular, the hole octahedrons. The black dashed lines represent the high symmetry directions Δ and S (XR) for which the experimental dispersions are given in (b) and (e). (c) and (d) Zooms of the Δ dispersion near the X point, showing the gap opening at X, respectively, at 370 K and 150 K. (e) Dispersion along the XR direction showing the splitting of the S bands. The dotted-dashed white lines in (d) and (e) represent the EDC displayed in (f), which enables to measure accurately the gap at X by fitting the two peaks (pseudo-Voigt fits in blue). The white lines are the calculated dispersions for commensurate AF Cr, with a scaling coefficient 0.58; the additional sections present in AF compared to paramagnetic Cr are underlined by dashed lines, the theoretical bands of symmetry not visible with the used polarization have a smaller thickness. The symmetry representations of the bands are indicated.

To shed light on these anomalies, the dispersion along the in-plane [$\bar{1}$10] direction with s polarization has been examined for different photon energies (and thus different k_{001}) in Figs. 6(b) and 6(c). Figure 6(b) is recorded at an incident photon energy of 71 eV, corresponding to a point in the Brillouin zone close to the Γ point (situated at $h\nu = 65$ eV). Thus we expect to observe only Σ_3 and Σ_1 bulk bands: some intensity can be readily ascribed to the Σ_3 band and its backfolding. Nevertheless, the presence of an intense feature (underlined by a violet dashed line) corresponds neither to a Σ band, nor to a surface state dispersion (that will be described in the following part). As can be seen in Fig. 4(c), this feature is not observed for the Cr experimental Σ direction, and the sole source of intensity near the Fermi level (the surface or interface

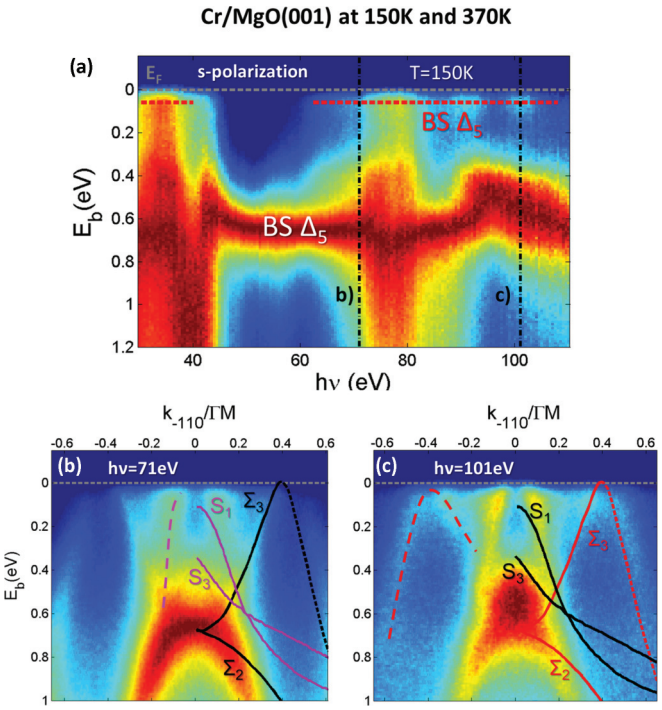

FIG. 6. (Color online) Measurements carried out with s polarization for out-of-plane wave vectors extracted from the measurements described in Fig. 2(c) for the Cr/MgO sample, at $T = 150$ K. (a) Dispersion along the normal direction with s polarization, as a function of the photon energy (Δ_5 symmetry bands alone are authorized). The red lines point out the presence of features near the Fermi level and the notation "BS" stands for bulk state. The black dash-dotted lines indicate the energies used for the in-plane dispersion scans displayed in (b) and (c). (b) Dispersion along the $[\bar{1}10]$ direction recorded at $h\nu = 71$ eV. (c) displays the same direction at $h\nu = 101$ eV. The expected dispersions for these photon energies are shown with black lines while additional dispersions are in color.

state marked SS1 and IS1) is not detected in s polarization. However, the dispersion of this feature matches well that of the S_1 band (corresponding to the dispersion in the $[\bar{1}10]$ direction from the X point). Moreover, the shift of intensity for $k_{\bar{1}10} = 0$ to lower binding energies (about 0.55 eV) can be explained by the presence of the S_3 band. This effect is also observed for $h\nu = 101$ eV (near the theoretical X point), in Fig. 6(c); along with features that can be ascribed to the expected S_1, S_3 bands and surface state, additional features are detected (underlined by a red dashed line), that fits well with the Σ_3 band and its AF backfolding.

These kinds of superimposed dispersions are very well observed (with different relative intensities for the two components) at all incident photon energies (but more easily detected above $h\nu = 70$ eV). They correspond to a projection in the normal direction of the dispersions along $[\bar{1}10]$. Therefore it is not possible to extract the dispersion with respect to k_{001}, as the resolution in the normal direction is lost. The possible origins of this phenomenon will be discussed in a following section.

Like for the Cr sample, characteristic AF features (folding of the Σ_3 band) persist at high temperature (nominally 370 K), above the bulk Néel temperature of 311 K (see Fig. 7). The superimposed dispersions are also still visible.

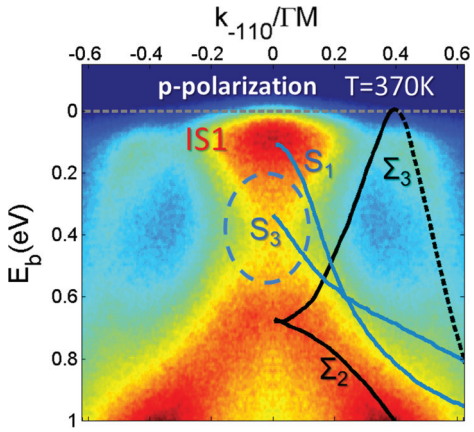

FIG. 7. (Color online) Dispersion with p polarization along the $[\bar{1}10]$ direction recorded at $h\nu = 71$ eV and $T = 370$ K. The expected dispersions for this photon energy are shown with black lines, while additional dispersions are in blue.

B. Surface/interface band structure

Aside from the bands described previously for Cr and Cr/MgO, additional features are observed: high-intensity zones near the Fermi level in Figs. 4(c), 4(d), and 4(f), respectively marked as SS1, IS1, and IS2 (SS stands for surface state and IS for interface state). We will demonstrate in this section that they are part of the Cr (001) surface and Cr(001)/MgO interface electronic structure.

A 2D localized state is usually identified by the flatness of its dispersion in the normal direction, or by its sensitivity to surface contamination (the peak disappears upon gas adsorption, or its binding energy varies). Our extended data set allows us to determine the binding energies of the surface state at different photon energies, not only in normal emission but also on a wide range of in-plane wave vectors. We are thus able to soundly establish their 2D character.

1. A localized state of Δ_1 symmetry just below the Fermi level

On the EDM in normal direction, for the Cr sample, a strong feature is observed at 51 meV (the standard deviation is 10 meV) below the Fermi level [see Fig. 8(a)]. This state is always fitted with a positive binding energy, corresponding to a filled state. Indeed, a temperature parameter far higher than the experimental temperature and a large peak width are required to obtain a negative binding energy in the fit. Since this feature keeps the same binding energy on the whole range where it can be fitted ($-0.45\Gamma X$ to $0.7\Gamma X$), we ascribe it to a surface localized state for which the normal wave vector resolution is thus lost.

Its dispersion along the in-plane $[\bar{1}10]$ direction is identical for the whole range of k_{001} given above, which is a solid proof of its 2D character. As displayed in Fig. 8(b), this state has a very flat dispersion near the zone center, which is typical of a strong d orbital character (like the Δ_5 bulk state near Γ). It reaches the Fermi level at $0.35\overline{\Gamma M}$, fairly near the value at which the paramagnetic Σ_3 bulk state intersects the Fermi level too.

This 2D localized state is identified in the Cr/MgO sample at a binding energy of 59 meV [the standard deviation (std)

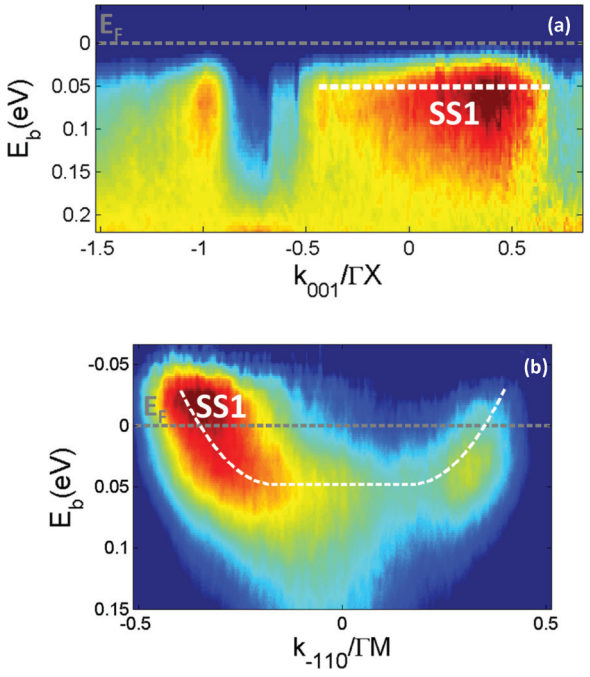

FIG. 8. (Color online) Surface features for the Cr sample at 150 K. (a) Zoom of the EDM in normal emission with p polarization, showing a nondispersive feature near E_F, marked as SS1 (surface state 1). (b) Dispersion of the surface state SS1 along the in-plane $\overline{\Gamma M}$ direction.

is 11 meV] as displayed in Fig. 9. The small difference with the binding energy value for Cr is inferior to the statistical error and thus not significant. The fitting of this state for the Cr/MgO sample is, indeed, made more complicated by the loss of resolution in the normal wave vector direction. We finally deduce that the surface state present on the Cr surface persists for a Cr/MgO interface, becoming an interface state.

Since it is not detected for normal emission with s polarization but is with p polarization, as featured on the EDC at Γ in Fig. 9, the symmetry of this localized state is Δ_1 along the ΓX

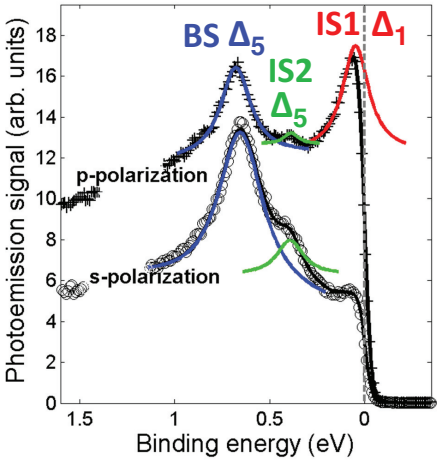

FIG. 9. (Color online) Energy distribution curve with s and p polarizations at the Γ point, for the Cr/MgO sample at 150 K, featuring the Δ_5 bulk state (BS) and the interface states (IS).

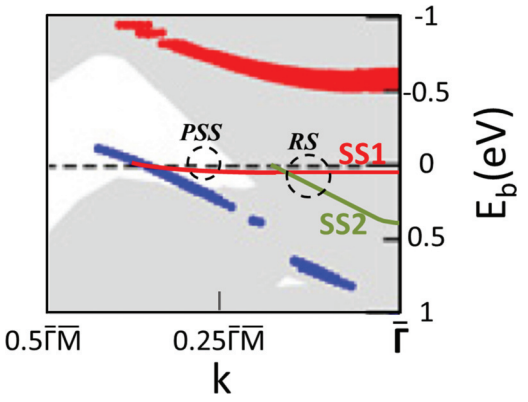

FIG. 10. (Color online) Calculated surface band dispersion along $\overline{\Gamma M}$ for up (blue) and down spins (red), the Cr(001) surface adapted projected bulk band structure is represented in gray (from Ref. 28). Experimental surface state dispersions: the red line, marked as SS1, is the dispersion of the low binding energy surface state and the green line, marked as SS2, that of the other surface state. PSS stands for pure surface state and RS for resonant state.

direction. The increase of the intensity near the Fermi level for p polarization with respect to s polarization gives an additional proof that the surface state survives in the Cr/MgO sample: the intensity near the Fermi level in Figs. 7 and 9 originates not only from the bulk Δ_5 state but also from the interface state, of symmetry Δ_1. At 370 K, this interface state is still detected, at a slightly higher binding energy ($E_b = 87$ meV, std: 17 meV). Besides, for the Cr sample, although the binding energy of the surface state cannot be accurately fitted on the whole range of k_{001} depicted in Fig. 8(a), the intensity near the Fermi level is always higher with p polarization than with s polarization, which proves the existence of the Δ_1 surface state near the Fermi level at any k_{001}.

Confronting the dispersion of this "Δ_1" surface state to the (001) surface projected band structure, it appears that it is situated in a bulk continuum apart for its section where it crosses the Fermi level. Thus this "surface state" is in fact a resonant state for most wave vector values, possibly becoming a true surface state (within the antiferromagnetic gap) near the Fermi level (see Fig. 10).

2. *A resonant localized state with Δ_5 symmetry*

On the EDC displayed in Fig. 9, an additional feature appears as a shoulder of the bulk Δ_5 state. Since it is situated at a binding energy close to the bulk state, it is difficult to detect (for the Cr/MgO interface state, $E_b = 0.39$ eV, std $= 0.03$ eV and for the bulk state, $E_b = 0.66$ eV). Moreover, the bulk state has a very flat dispersion near Γ, making it difficult to discriminate from the 2D state. The localized state appears nonetheless clearly at the same binding energy on a wide range of k_{001} values, for Cr and Cr/MgO samples, comforting the assumption of its 2D localized nature. This state is assigned to Δ_5 symmetry along the Δ direction since it is present for both s and p polarizations.

This state is identified in the Cr sample by its characteristic dispersion featured in Fig. 11(a), which stays identical on its entire range of detection. This dispersion is very steep along $\overline{\Sigma}$ but also along $\overline{\Delta}$ [from what can be observed in Fig. 4(f)],

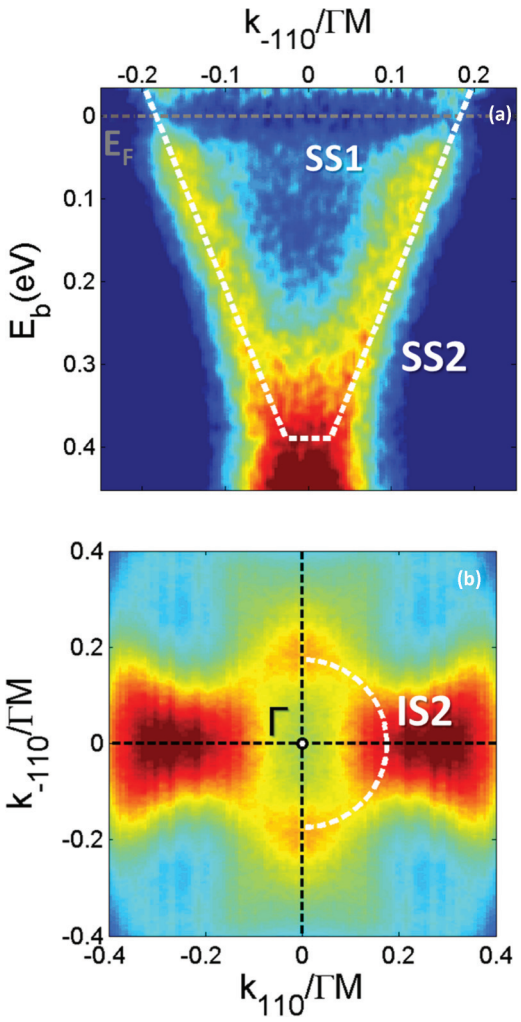

FIG. 11. (Color online) (a) Dispersion along $\overline{\Sigma}$ of the surface state (marked as SS2) recorded at 150 K for the Cr sample. It has been obtained by summing the dispersions with p polarization on the k_{001} range of detection of the feature. (b) Fermi surface (001) section for the Cr/MgO sample with p polarization featuring the interface state IS2 Fermi surface.

corresponding to high group velocities at the Fermi level and to a strong sp orbital character.

Within experimental errors, the dispersion and binding energies are fairly similar in Cr and Cr/MgO, and from confrontation with the (001) surface projected bulk bands, this state is deduced to be a resonant state on its entire wave vector range (see Fig. 10). In Cr/MgO, the Fermi surface of this interface resonant state displayed in Fig. 11(b) appears clearly as a square centered at Γ. At higher temperature (370 K), the surface and interface states are still well detected, but owing to thermal broadening of the bulk state, no binding energy value can be reliably determined.

V. DISCUSSION

A. Bulk band structure and magnetism

Our study provides detailed and additional material to previous works on the Cr bulk electronic band structure[8,29–34,51] and, in particular, high-resolution data for the low binding energy dispersions (see Table II). In the chosen energy range, the 3-step model with direct transition is accurate, except for energies below 30 eV. Such an effect was also observed previously for the Cr(110) surface in normal emission.[31,32] Our work is consistent with recent studies finding that the experimental binding energies are smaller than those obtained by calculations. The discrepancy of energies obtained by self-consistent calculations with local density approximation (like that used here, of Skriver *et al.*[16]) is a usual problem for metals, but it can be solved partially thanks to many-particle corrections.[52] The accurate value of 0.68 eV (instead of about 1 eV) for the Γ'_{25} binding energy can thus be retrieved.

Another point of disagreement with calculations is the shape of the Σ_1 band, which, from our measurements, is merged with the Σ_2 theoretical band at small wave vectors. This dispersion matches well that proposed by Kulikov *et al.*[52,53] (where this bending appears only for AF Cr) but fits less with earlier ones.[15,16,18] It led authors to ascribe these features (belonging to Σ_1 symmetry) to the symmetry forbidden Σ_2 band and to attribute the failure of the dipolar rules in normal emission to a bad resolution of the detection angle.[31,32]

Magnetism is another important stumbling block for *ab initio* calculations: the incommensurate SDW is never found as a ground state, commensurate AF is sometimes predicted but for an underestimated lattice parameter and with inaccurate values of the magnetic moment. This impacts directly the band structure shape through the energy width g of the accidental gaps ($g = J_{\text{eff}} m_b$, J_{eff} being the effective Stoner interaction parameter). With the usual value for J_{eff} of 0.8 eV, see Ref. 21, and the experimental bulk moment value of $0.54\mu_B$, a gap of 0.41 eV is expected for commensurate AF and twice as less for an SDW order. The value of 0.21 eV for the accidental gap along Σ reported by Schäfer *et al.* at 300 K for a Cr(110) surface is in very good agreement with this Stoner parameter value.[51] As our photoemission measurements and the chosen temperature do not enable us to investigate the states at sufficient high energy above the Fermi level, we have studied the gap at X, which does not directly participate to the stabilization of the SDW order. Although it cannot directly be related to the Stoner parameter, the magnitude of this gap is, however, also a good probe of the Cr magnetism and of its evolution with temperature: it shall reach zero at the Néel temperature.

As demonstrated previously, the Cr sample is in an AF state (there is a gap opening at X), even if the characteristic Σ_3 folding is not observed in the ΓM direction. It is hence possible that the nesting does not need to be perfect for the AF order to exist, and that large sections of the octahedron can remain unnested (here in the in-plane direction). For the Cr/MgO sample, on the contrary, the in-plane dispersions are clearly characteristic of a good nesting on the Fermi surface. In particular, the difference of dimension of the electron and the hole octahedron dimension along ΓM is 0.11 Å^{-1} (see Table II). The value thus obtained for the nesting vector $\vec{Q}'_{\pm} = (1 \pm \delta)\langle 001 \rangle$ (with $\delta = 0.036$) is consistent with experimental measurements of the nesting vector and of its dependence on temperature and film thickness by Rotenberg

et al., recalling that the nesting vector may differ slightly from the SDW vector.[42]

There are three symmetry equivalent orientations of the propagation vector of the SDW, and thus of the nesting vector, along the axes ⟨100⟩ of the cubic lattice. A unique orientation is nevertheless sufficient to induce a nesting of the whole hole and electron octahedra, so that there is only one direction of nesting and propagation of the SDW at a time.[21] Subtle differences shall occur on the Fermi surface on the holes ellipsoids at M and electron balls at X but thermal broadening (and symmetry selection) prevented us to observe them. On a larger scale (that of the whole film: 100 nm×sample area), neutron diffraction gives access to both propagation direction and polarization of the SDW, and from our experience of Cr(001) thin films grown on a MgO(001) substrate with the very same growth recipe, the magnetic phase in such samples is an out-of-plane propagating transverse SDW, for epitaxial strain reasons.[12]

Contrary to macroscopic probes of the AF order (resistivity measurements, neutron or x-ray diffraction), which identify for our Cr thin films signs of the Néel transition near 311 K or below, the surface sensitive measurement provided by ARPES (on a few atomic monolayers) shows characteristic AF features far above the macroscopic Néel temperature. Indeed, at 370 K, the gap at X is still opened (though smaller than at 150 K) for the Cr sample, and the AF folding of the Σ_3 band persists for the Cr/MgO sample. A strain and defect stabilized commensurate AF phase is known to persist at very high temperature, far above the Néel temperature of 311 K.[21] However, neutron diffraction measurements in Cr films grown with the same recipe always demonstrated the absence of this phase, thanks to the high-temperature annealing of the film.[12] For the Cr(110) surface, an investigation of the Fermi surface and of the accidental gap width determined a surface T_N of 440 K.[51] For the Cr(001) surface, the existence of a near surface order AF at high temperatures was first claimed by Klebanoff *et al*. at temperatures as high as three times the bulk Néel temperature,[54] while Sakisaka found clues for a PM phase at 470 K.[32] Our study deduces the existence of an AF phase at 370 K. The persistence of a high temperature near-surface AF order seems hence to be a general feature of Cr surfaces (for different orientations). It could be stabilized by enhanced surface magnetic moments as theoretically predicted for the Cr(001) surface[22,23] (discussed in more details in another article[9]) or arise from a short-range magnetic order as proposed by Klebanoff *et al*.[54] Local bulk magnetic moments are known to persist above the Néel temperature and could be AF correlated at small time and space scales, as that investigated in ARPES (like in the case of NiO[55]).

B. Metal induced gap states in Cr/MgO?

We will now focus on the main differences between the band structures for Cr and MgO-covered Cr: namely the loss of normal wave vector resolution observed for the Cr/MgO sample for normal emission and (110) mirror plane emission. The scans show the superposition of the typical dispersion along ΓM (corresponding to $k_{001} \equiv 0[4\pi/a]$) and XR (corresponding to $k_{001} \equiv \pi/a[2\pi/a]$), evidencing a loss of resolution in k_{001} larger than π/a (as demonstrated by Fig. 6).

This loss of the normal wave vector component could happen during the escape of photoelectrons from the MgO. The presence of MgO on the Cr layer could alter the value of the work function ϕ for the Cr/MgO sample and the MgO layer roughness lead to a distribution of ϕ values at the scale of the incident beam size (50 μm). However, to explain the observed resolution loss (more than half an AF BZ), a large distribution of (not physical) ϕ values would be necessary. On the contrary, Fermi-Dirac distributions show no such difference between the Cr and the Cr/MgO sample in the ϕ value (change of about 0.1 eV) and in the fitted temperature. This normal wave vector loss cannot either originate from an (important) alteration of the band structure of the Cr layer once covered by MgO. Indeed, our scans at constant photon energy (60 eV) show no qualitative differences between the PM part of the measured band dispersions for Cr and Cr/MgO, and the X point on the normal emission scans is situated near 33 eV for both samples. The same value for the inner potential (and E_0) is thus valid for both samples.

We propose that the additional features that show no resolution in k_{001} originate directly from the MgO layer. These bands are not part of the MgO band structure (the investigated binding energies lie in the MgO gap), but are created by Cr bulk states that become evanescent states in the MgO layer (the so-called metal-induced gap states, MIGS[56–58]). The cubic symmetry is conserved throughout our epitaxial Cr/MgO stack, thus metallic wave functions with Δ symmetry can connect with evanescent wave functions of same symmetry in the barrier. As pointed out by Butler *et al*.[56] and Diederichs *et al*.,[58] the attenuation rate of the Δ wave functions is determined by the complex band structure of the insulator: in MgO, Δ_1 and Δ_5 wave functions undergo the smaller attenuation. As a rule of thumb, wave functions with less nodes in the (001) planes are less attenuated in MgO, and thus wave functions with strong s orbital character are better transmitted than those with strong p and d character. For off-normal wave functions, the attenuation increases largely (though not exponentially as expected) with the in-plane wave vector component $k_{\parallel}$.[56]

The participation of MIGS to the intensity of the Cr bulk band would explain two characteristics of the effect observed on the Cr/MgO sample (cf. Fig. 6), namely, the superimposition of the dispersion near ΓM and XR in the $k_{\bar{1}10}$ direction, which denotes a resolution loss in k_{001}, and the increase of this effect from a photon energy of 60 eV. At the Cr/MgO interface, the in-plane component is conserved but not the normal component of the electron wave vector. Additionally, as the MIGS is extremely localized in depth (the wave-function amplitude decreases exponentially), it should show no normal wave vector dependence of the binding energy, similarly to a surface state. These statements shall be verified for normal emission ($k_{\parallel} = 0$) but also for small $k_{\parallel}$ components. Besides, the features at low binding energy shall be the best transmitted in the MgO, which explains the easy detection of the low binding part of the XR dispersion giving enhanced signal near the Fermi level in Fig. 6(a). We therefore ascribe the superimposition of different dispersions along $k_{\bar{1}10}$ in Cr/MgO to the signal stemming from MIGS in MgO.

We now explain the enhancement of the effect with respect to the photon energy. On one side, the evolution of the

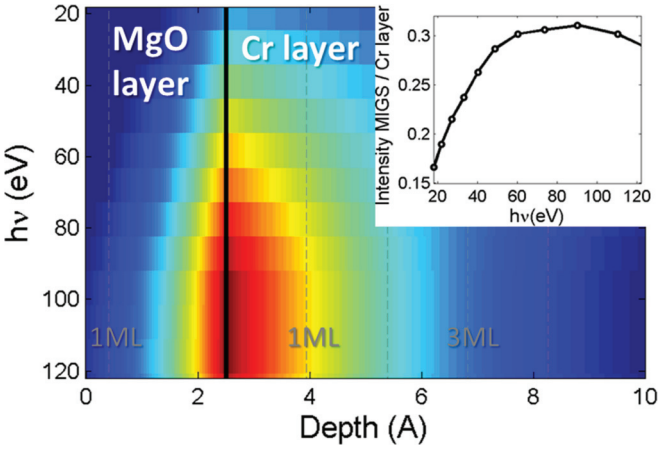

FIG. 12. (Color online) Depth-resolved contribution of the intensity of a bulk band as a function of the incident photon energy $h\nu$. Only the dependence of the photoelectron depth on hν and the attenuation of a Δ_5 bulk band in MgO (by $\kappa = 0.81$ Å^{-1}, see Ref. 56) have been taken into account in this sketch. The intensity at each $h\nu$ is normalized to the contribution of the Cr layer to the intensity.

escape depth (see Fig. 3) for increasing photon energies favors photoelectron signal stemming from a lower depth in the film: the most weight of the signal is hence displaced near the Cr interface. On the other side, the existence of MIGS decaying in the MgO layer favors the contribution from near-interface regions in MgO. The combined effect of these two contributions is represented in Fig. 12: the contribution of the interface region becomes more prominent with increasing photon energy and that of the signal coming from MgO is doubled from 20 to 60 eV, and saturates above 60 eV. This is in agreement with the easier detection of the superimposition of the bands above 60 eV, in Fig. 6(a). We thus ascribe the features observed in the Cr/MgO sample for normal emission and (110) mirror plane emission (in Fig. 6) to the superposition of the Cr bulk bands dispersions in the Cr layer and of the Cr evanescent bands in the MgO layer whose contribution is strengthened at high photon energies.

C. Δ_1 localized state and surface/interface magnetism

From our measurements, we have deduced the existence of a surface state on the Cr(001) surface that persists as an interface state at the Cr/MgO interface. It is situated at a very low binding energy (which increases slightly with temperature) and shows a flat dispersion along the $\overline{\Sigma}$ direction, corresponding to a strong d orbital character. It possesses Δ_1 symmetry (with a strong d_{z^2} orbital component) along Δ. By comparing this information with theoretical calculations (tight binding[25] and DFT[26,28]), this localized state is identified with certainty as a minority surface state situated above the Fermi level (about 1 eV) in all calculations. Its reported experimental binding energy differs slightly from a work to another (probably because of different levels of surface cleanliness) and its symmetry has been debated (see Ref. 9 and references therein). We provide here additional solid proofs of its Δ_1 symmetry, and an accurate measurement of its experimental dispersion.

According to early calculations on the Cr(001) surface,[22,23] the enhancement of the density of states at the surface is at the origin of a ferromagnetic ordering on the Cr surface plane. The surface moments are enhanced relative to the bulk value (up to $3\mu_B$ instead of $0.42\mu_B$) and the splitting of the polarized surface states is proportional to the surface moments. The magnitude of surface and Cr/MgO interface moments has been discussed in a separate article,[9] by confronting our information on this polarized state and polarized neutron reflectivity measurements. We have concluded that the surface/interface atoms bear a noncompensated magnetization that is very weak compared to computational predictions (about ten times less).

Like the Δ_5 surface state evidenced on the Fe(001) surface,[59] it is not a pure surface state at all wave vector values, becoming a surface resonance when it crosses bulk bands (recall Fig. 10). However, it is the only state of this symmetry representation at these binding energies. It is particularly relevant for the Cr/MgO interface and for Cr/MgO epitaxial stacks since the symmetry is conserved throughout the stack and since Δ_1 states are the least attenuated states in the barrier ($\kappa = 0.33$ Å^{-1}).[56] Hence, for the symmetry-resolved MgO barrier, this state is a true interface state and shall bring an interface-localized but significant contribution in polarized transport to the minority channel. As Cr has no Δ_1 state at the Fermi level, a lot of studies regard it as a Δ_1 symmetry filter,[10,11] however, this approximation may be faulted especially for very thin Cr layers,[11] where Δ_1 interface states shall play a significant role in tunnel transport.

D. Δ_5 resonant state and transport

The linear dispersion along $\overline{\Gamma M}$ (and also $\overline{\Gamma X}$) of the Δ_5 state shows a strong similarity with that of a majority surface state situated at 1 eV binding energy at $\overline{\Gamma}$ according to calculations (see Fig. 10). It is not surprising that, as for bulk states, the binding energy obtained with calculations is inaccurate. This localized state is most likely the same as that featured at 0.5 eV (binding energy) in the normal emission photoemission study of the Cr(001) surface by Budke *et al.*.[41] However, the only proof they provided for its localized nature was its sensitivity to contamination.

The identification of this state also allows us to explain contradictory results in the literature: in addition to the Δ_1 surface state, Klebanoff *et al.* exhibited a Δ_5 feature at 0.63 eV binding energy, strongly affected upon CO exposure.[54,60] They attributed this state to a surface resonance. They also deduced the magnitude of the surface ferromagnetic moment and its surface Curie temperature from the energy difference of these two states. Later, through normal emission measurements, Nakajima *et al.* evidenced the dispersion of the feature previously observed at 0.63 eV,[33] which is that of the very Δ_5 bulk state featured in this study, and hence contradicted their interpretation. We believe that Klebanoff *et al.* actually observed both the surface and the bulk state (and were not able to discriminate them because of lack of energy resolution). Nevertheless, as their two surface states are of different symmetries, they shall not be exchange-splitted states arising from one surface state in the paramagnetic phase.

The better detection of the Δ_5 localized state in Cr/MgO may originate from the existence of an associated MIGS in the MgO barrier, like for the Δ_5 bulk state [compare Fermi surfaces in Figs. 4(a) and 4(b)]. The Δ_1 state seems also to be

enhanced, but the intensity near E_F levels coming from XR dispersions does not allow us to compare.

In addition, this resonant state crosses the Fermi level for low in-plane wave vector values so the transmission of the MgO barrier may be only slightly dampened even near the Fermi level (thanks also to the strong sp orbital character of this state). For tunnel transport in a Cr/MgO/Cr epitaxial system, a hot spot contribution of this interface resonant state that forms a ring around the Γ point may be expected, similarly to what has been calculated for the Fe/MgO/Fe system.[56,58]

Finally, as this state is partially transmitted through thin MgO barriers (1–3 ML) and is resonant with bulk states that play an important role in the stabilization of the SDW order in Cr, it has been proposed to be a vector of the tunnel coupling observed in Cr/MgO/Cr, similarly to Fe/MgO/Fe systems.[12]

VI. CONCLUSION

To conclude, we have presented in this article a detailed and thorough study of the bulk and surface/interface low-energy electronic structure for a Cr(001) layer covered or not with MgO. The experimental dispersions that we present for the Cr volumic bands are very close to that of the theoretical band structure, at the notable exception of the binding energies that are overestimated by calculations, and of the shape of the Σ_1 dispersion. Moreover, we have evidenced characteristic AF features like the AF gap at the X point, and the backfolding of the Σ_3 band at the electrons octahedron edge (in the Cr/MgO sample). We have shown that these AF characteristics persist above the Néel temperature of bulk Cr at 311 K. Our precise results on the electronic structure and magnetism that agree qualitatively with theoretical calculations may be useful to optimize the calculation methods on our model itinerant AF.

Besides, for the Cr(001) surface, we have established the existence of a Δ_5 surface resonance at 0.39 eV below the Fermi level, and of a Δ_1 state at 0.05 eV below the Fermi level that becomes a pure surface state as it crosses the Fermi level. We have presented their in-plane dispersion. These localized states persist with the same properties at a Cr/MgO interface, which is also a proof of the quality and absence of oxidation at our metal/oxide interface. It may be an important step forward for calculations to be able to reproduce these interface characteristics, in the prospect of simulating transport in a complete heterostructure.

We have ascribed experimental peculiarities, occurring only when the Cr layer is covered with 1.2-ML MgO, to the presence of MIGS in the MgO layer, that stem from the attenuation of bulk and interface states in the barrier. This information on the electronic properties of Cr/MgO interfaces shall also be meaningful for the understanding of polarized transport and coupling not only for Cr/MgO stacks but also for other bcc metal/MgO epitaxial systems.

ACKNOWLEDGMENTS

This work was supported by the French Agence Nationale de la Recherche, ANR-11-JS10-005 “ELECTRA.” We are thankful to Amina Neggache for her help with the ARPES experiment and samples growth. M.-A. L. thanks Gaston Exil for technical support. We are grateful to C. Barreteau for fruitful discussions.

[1] M. N. Baibich, J. M. Broto, A. Fert, F. Nguyen Van Dau, F. Petroff, P. Etienne, G. Creuzet, A. Friederich, and J. Chazelas, Phys. Rev. Lett. **61**, 2472 (1988).
[2] M. D. Stiles, Phys. Rev. B **48**, 7238 (1993).
[3] P. Bose, P. Zahn, I. Mertig, and J. Henk, J. Electron Spectrosc. Relat. Phenom. **182**, 97 (2010).
[4] Y. S. Dedkov, Eur. Phys. J. B **57**, 15 (2007).
[5] D. Li, J. Pearson, S. D. Bader, E. Vescovo, D.-J. Huang, P. D. Johnson, and B. Heinrich, Phys. Rev. Lett. **78**, 1154 (1997).
[6] R. Hafner, D. Spisak, R. Lorenz, and J. Hafner, Phys. Rev. B **65**, 184432 (2002).
[7] S. Cottenier, B. De Vries, J. Meersschaut, and M. Rots, J. Phys.: Condens. Matter **14**, 3275 (2002).
[8] E. Rotenberg, O. Krupin, and S. D. Kevan, New J. Phys. **10**, 023003 (2008).
[9] M.-A. Leroy, A. M. Bataille, M. Fitzsimmons, Q. Wang, F. Bertran, F. Ott, T. Hauet, C. Gatel, and S. Andrieu (unpublished); M.-A. Leroy, Ph.D. thesis, Université de Lorraine, 2013 (in French).
[10] F. Greullet, C. Tiusan, F. Montaigne, M. Hehn, D. Halley, O. Bengone, M. Bowen, and W. Weber, Phys. Rev. Lett. **99**, 187202 (2007).
[11] R. Matsumoto, A. Fukushima, K. Yakushiji, S. Nishioka, T. Nagahama, T. Katayama, Y. Suzuki, K. Ando, and S. Yuasa, Phys. Rev. B **79**, 174436 (2009).
[12] M.-A. Leroy, A. M. Bataille, B. Dkhil, F. Porcher, A. Barbier, V. Jacques, Y. Lu, C. Bellouard, T. Hauet, S. Ravy *et al*. [Phys. Rev. B (to be published)].
[13] P. M. Haney, D. Waldron, R. A. Duine, A. S. Núñez, H. Guo, and A. H. MacDonald, Phys. Rev. B **75**, 174428 (2007).
[14] A. M. Turner, A. W. Donoho, and J. L. Erskine, Phys. Rev. B **29**, 2986 (1984).
[15] D. G. Laurent, J. Callaway, J. L. Fry, and N. E. Brener, Phys. Rev. B **23**, 4977 (1981).
[16] H. Skriver, J. Phys. F: Met. Phys. **11**, 97 (1981).
[17] W. M. Lomer, Proc. Phys. Soc. **80**, 489 (1962).
[18] S. Asano and J. Yamashita, J. Phys. Soc. Jpn. **23**, 714 (1967).
[19] C. Windsor, J. Phys. F: Met. Phys **2**, 742 (1972).
[20] S. A. Werner, A. Arrott, and H. Kendrick, Phys. Rev. **155**, 528 (1967).
[21] E. Fawcett, Rev. Mod. Phys. **60**, 209 (1988).
[22] G. Allan, Surf. Sci. **74**, 79 (1978).
[23] D. R. Grempel, Phys. Rev. B **24**, 3928 (1981).
[24] S. Blugel, D. Pescia, and P. H. Dederichs, Phys. Rev. B **39**, 1392 (1989).
[25] H. Hasegawa, J. Phys. F: Met. Phys. **16**, 1555 (1986).
[26] C. L. Fu and A. J. Freeman, Phys. Rev. B **33**, 1755 (1986).
[27] R. H. Victora and L. M. Falicov, Phys. Rev. B **31**, 7335 (1985).

[28]P. Habibi, C. Barreteau, and A. Smogunov, J. Phys.: Condens. Matter **25**, 146002 (2013).
[29]G. Gewinner, J. C. Peruchetti, A. Jaéglé, and R. Pinchaux, Phys. Rev. B **27**, 3358 (1983).
[30]L. E. Klebanoff, R. H. Victora, L. M. Falicov, and D. A. Shirley, Phys. Rev. B **32**, 1997 (1985).
[31]L. I. Johansson, L. G. Petersson, K. F. Berggren, and J. W. Allen, Phys. Rev. B **22**, 3294 (1980).
[32]Y. Sakisaka, T. Komeda, M. Onchi, H. Kato, S. Suzuki, K. Edamoto, and Y. Aiura, Phys. Rev. B **38**, 1131 (1988).
[33]N. Nakajima, O. Morimoto, H. Kato, and Y. Sakisaka, Phys. Rev. B **67**, 041402 (2003).
[34]O. Krupin, E. Rotenberg, and S. D. Kevan, Phys. Rev. Lett. **99**, 147208 (2007).
[35]J. Schäfer, E. Rotenberg, S. Kevan, and P. Blaha, Surf. Sci. **454**, 885 (2000).
[36]J. E. Graebner and J. A. Marcus, Phys. Rev. **175**, 659 (1968).
[37]J. A. Stroscio, D. T. Pierce, A. Davies, R. J. Celotta, and M. Weinert, Phys. Rev. Lett. **75**, 2960 (1995).
[38]M. Kleiber, M. Bode, R. Ravlić, and R. Wiesendanger, Phys. Rev. Lett. **85**, 4606 (2000).
[39]T. Hänke, M. Bode, S. Krause, L. Berbil-Bautista, and R. Wiesendanger, Phys. Rev. B **72**, 085453 (2005).
[40]O. Y. Kolesnychenko, G. M. M. Heijnen, A. K. Zhuravlev, R. de Kort, M. I. Katsnelson, A. I. Lichtenstein, and H. van Kempen, Phys. Rev. B **72**, 085456 (2005).
[41]M. Budke, T. Allmers, M. Donath, and M. Bode, Phys. Rev. B **77**, 233409 (2008).
[42]E. Rotenberg, B. K. Freelon, H. Koh, A. Bostwick, K. Rossnagel, A. Schmid, and S. D. Kevan, New J. Phys. **7**, 114 (2005).
[43]W. Weber, D. A. Wesner, D. Hartmann, and G. Güntherodt, Phys. Rev. B **46**, 6199 (1992).
[44]O. Rader, E. Vescovo, J. Redinger, S. Blügel, C. Carbone, W. Eberhardt, and W. Gudat, Phys. Rev. Lett. **72**, 2247 (1994).
[45]M. Schmid, M. Pinczolits, W. Hebenstreit, and P. Varga, Surf. Sci. **377**, 1023 (1997).
[46]J. Hermanson, Solid State Commun. **22**, 9 (1977).
[47]W. Eberhardt and F. J. Himpsel, Phys. Rev. B **21**, 5572 (1980).
[48]A. Damascelli, Phys. Scr., T **109**, 61 (2004).
[49]F. Reinert and S. Hüfner, New J. Phys. **7**, 97 (2005).
[50]S. Tanuma, C. J. Powell, and D. R. Penn, Surf. Interface Anal. **43**, 689 (2011).
[51]J. Schäfer, E. Rotenberg, G. Meigs, S. D. Kevan, P. Blaha, and S. Hüfner, Phys. Rev. Lett. **83**, 2069 (1999).
[52]N. I. Kulikov, M. Alouani, M. A. Khan, and M. V. Magnitskaya, Phys. Rev. B **36**, 929 (1987).
[53]N. I. Kulikov and E. T. Kulatov, J. Phys. F: Met. Phys. **12**, 2291 (1982).
[54]L. E. Klebanoff, S. W. Robey, G. Liu, and D. A. Shirley, Phys. Rev. B **31**, 6379 (1985).
[55]A. Barbier, C. Mocuta, W. Neubeck, M. Mulazzi, F. Yakhou, K. Chesnel, A. Sollier, C. Vettier, and F. de Bergevin, Phys. Rev. Lett. **93**, 257208 (2004).
[56]W. H. Butler, X.-G. Zhang, T. C. Schulthess, and J. M. MacLaren, Phys. Rev. B **63**, 054416 (2001).
[57]P. Mavropoulos, N. Papanikolaou, and P. H. Dederichs, Phys. Rev. Lett. **85**, 1088 (2000).
[58]P. H. Dederichs, P. Mavropoulos, O. Wunnicke, N. Papanikolaou, V. Bellini, R. Zeller, V. Drchal, and J. Kudrnovský, J. Magn. Magn. Mater. **240**, 108 (2002).
[59]L. Plucinski, Y. Zhao, C. M. Schneider, B. Sinkovic, and E. Vescovo, Phys. Rev. B **80**, 184430 (2009).
[60]L. E. Klebanoff, S. W. Robey, G. Liu, and D. A. Shirley, Phys. Rev. B **30**, 1048 (1984).